# Pre and post-diction simulation of the seismic response of a masonry cross vault tested on a shaking table

Daniele Pellegrini[a]

[a] *Institute of Information Science and Technologies "A. Faedo" (ISTI-CNR), Pisa, Italy*

e-mail: daniele.pellegrini@isti.cnr.it

# Pre and post-diction simulation of the seismic response of a masonry cross vault tested on a shaking table

Masonry vaults are widely employed in ancient constructions and play a crucial role in their static and dynamic behaviour. In the last decades, the scientific community has carried out, on the one hand, several experimental campaigns aimed at characterising the response of masonry vaults to horizontal actions; on the other, it has developed sophisticated numerical models able to catch the crucial features of their structural response. Within the framework of the SERA.TA project (Seismology and Earthquake Engineering Research Infrastructure Alliance for Europe), pre and post-diction contests have been organised to assess the capability of numerical methods to predict the seismic response of a 1:1 scale model of a masonry cross vault, realised and tested at LNEC laboratory (Portugal). This paper outlines the numerical analyses performed on some vault models within the pre and post-diction phase of the project. The numerical models have been created and analysed with NOSA-ITACA, a finite element software implemented at ISTI−CNR and devoted to the structural analysis of ancient masonry constructions. Pros and cons of the numerical simulations have been analysed, comparing the prediction and post-diction results with the experimental data in terms of accelerations, displacements, and crack patterns. Numerical results fit the experimental outcomes, and betterment is evident in the post-diction phase.

Keywords: masonry vault; groin vault; model updating; nonlinear elasticity; masonry-like material; nonlinear dynamic analysis

## 1. Introduction

Masonry vaults can efficiently withstand vertical loads but exhibit a high fragility against seismic actions. Their structural analysis and safety assessment represent a challenging

task due to several factors, such as the material nonlinearities (low tensile strength and limited compressive resistance) and uncertainties affecting masonry structures about boundary conditions, material properties, infill, load history, construction process, presence of previous damages, and state of maintenance.

In the last decades, the scientific community addressed this issue carrying out, on the one hand, experimental campaigns aimed at characterising the behaviour of masonry vaults regarded as macro-elements and, on the other, developing sophisticated numerical models able to catch the crucial features of their structural response. Focusing on groin vaults (often used to cover churches' naves and palaces' rooms), the most frequent cause of failure is represented by support displacements resulting in a shearing action in the horizontal plane. Although this structural typology is widely spread worldwide, only some researchers have conducted full experimental campaigns on the shear behaviour of masonry vaults. A review of the principal experimental tests carried out, and an extensive collection of references are provided in (Bianchini et al. 2022). An experimental campaign was conducted by Silvestri et al. (2021) within the SEBESMOVA3D project. In this campaign, the authors investigated the seismic response of a 2 m × 2 m in plan groin vault made of filled 3D-printed plastic blocks and dry joints. Two support boundary conditions involving four lateral confinement modes were tested by applying, through a shaking table, seismic actions in one horizontal direction up to collapse. As a result, the vault showed a strong non-linear behaviour, characterised by a decrease of the fundamental frequency and increase of damping with increasing accelerations.

From a numerical point of view, plenty of approaches were developed to examine the structural behaviour of masonry structures ranging from limit analysis to Finite Element Method (FEM) and Discrete Element Method (DEM) (Gaetani 2020; Cattari et al. 2022). Nowadays, FEM is one of the most adopted procedure for structural analysis, with a large

set of constitutive equations capable of modelling the masonry construction response. This collection can be divided into two large groups. The first one gathers equations in which the material macroscopic behaviour is the result of micro-mechanical behaviours of the distinct components (Stefanou et al. 2015; Bertolesi et al. 2016; Regan et al. 2017; Petracca 2017). The second group, instead, contains all those constitutive equations that model masonry material as an equivalent continuum (Lucchesi et al. 2008; Nodargi and Bisegna 2019; Bilko and Małyszko 2020; Lourenço and Gaetani 2022), or as an assemblage of macro elements with few degrees of freedom and a pre-established behaviour (Malomo and DeJong 2022; Cattari et al. 2022; Vadalà et al., 2022). In this last group, it is also possible to include those models initially formulated for the concrete material and later applied to masonry structures. An exhaustive review of the formulated models is outside the scope of the present work, and the reader is referred to (Cattari et al. 2022) for more details.

Analyses carried out through DEM are also gaining ground. Indeed, DEMs provide a numerical representation of masonry structures as an assembly of discrete units (deformable or not) interacting along joints. In this way, it is possible to consider the internal arrangement of the components and their material properties, which can influence the static and dynamic response of the construction (Sarhosis et al., 2019; Pulatsu et al., 2020; Masi et al., 2020).

Within the framework of the FEM approach, the maximum modulus eccentricities surface (MMES) proposed by Lucchesi et al. (1999) is a useful tool for studying masonry arches and vaults modelled using the constitutive equation of *masonry-like* materials and shell elements. Such a surface plays a crucial role in studying the safety of masonry arches, vaults and domes subjected to any static load; as long as it is well contained in the structure's thickness, a safety margin is always guaranteed. Furthermore, MMES allows

the calculation of the collapse multiplier for different types of loads.

D'Altri et al. (2017) analysed the Giulio II cross vault in Italy, which suffered severe damage from the 2012 Emilia earthquake, developing a detailed finite element model, including its bearing tower. The results of non-linear static and dynamic analyses, carried out considering the Concrete Damage Plasticity (CDP) model for masonry material, were compared to the vault's crack pattern and the deformed geometry surveyed, showing a good agreement with the significant cracks suffered by the vault. Furthermore, the study highlighted the importance of considering vault-bearing structures within the FE model. The CPD model was also employed by Carfagnini et al. (2018) to reproduce the experimental results concerning a cross-masonry vault scaled model, tested by applying a shear displacement through the two supports moving. The linear and non-linear FE simulations confirmed the experimental crack pattern, the uplift of the vault, the shear deformation along the ribs and the asymmetric deformation (rotation). Milani et al. (2019) applied the CDP model to simulate the experimental results of tests performed on a 1:5 scale model of a groin vault tested under horizontal loads up to collapse (Fagone et al., 2016). Another non-linear model consisting of rigid elements and elastoplastic interfaces (with softening) was considered. The structure's arches were modelled with a heterogeneous approach, and the material constituting the vault was assumed to be isotropic with quasi-zero tensile strength and softening behaviour. All the models agreed with experimental load-carrying capacity prediction and failure mechanism results. In (Bianchini et al. 2019), the authors summarised the results of numerical analyses conducted on a full-scale model of a brick masonry groin vault characterised by asymmetric boundary conditions before performing shake table tests. All numerical simulations were performed using a Total-Strain Rotating Crack Model. The direct comparison among non-linear static, dynamic and Incremental Dynamic Analysis (IDA)

results led to considerations about the goodness of the mock-up developed and a prediction of the expected results from the execution of the experimental tests. Lastly, Alforno et al. (2022) showed parametric analyses' results on the masonry cross vaults' seismic response when the bricks grid varies. The FE model was built considering two brick patterns and two lateral boundary conditions. The bricks were assumed to be linear elastic, while interface elements with assigned tangential frictional behaviour and normal rigid compressive contact modelled joints. The free detachment was allowed under traction. Nonlinear static analyses were performed, assuming two different directions of the seismic input. The analysis showed that the brick pattern greatly influences the vault seismic response regarding peak load factor and maximum displacement.

As far as the DEM approach is concerned, its application to cross vaults is recent and rather limited. Van Mele et al. (2012) applied the Discrete Element method to simulate the response of a small-scale cross vault tested in the laboratory and subjected to large displacements. The computational model, built via 3DEC software based on the contact formulation of Cundall and Strack (1979), used rigid blocks and contact joints with assigned normal and shear stiffness. The experimental and numerical results were comparable even if the numerical model generally overestimated the displacement capacity; this circumstance was attributed to the fact that the DE model is a 'perfect' assembly of 'perfect' blocks and contact surface, thus resulting in perfect blocks interlocking. Lengyel et al. (2018) and Foti et al. (2018) adopted the same approach and software to analyse the structural behaviour of cross vaults. The former analysed the ribs' influence on groin vaults subjected to seismic load under the assumption of deformable blocks and dry connections. The analyses results, given in terms of damage, natural frequencies and internal force highlighted that (i) the ribbed vault was less vulnerable compared to one without reinforcements; (ii) the system's fundamental frequency was

much smaller than the initial one after seismic action; and finally, (iii) during the shock, the vault behaviour was similar to that of a barrel vault. Foti et al. (2018) compared the experimental and numerical response of a cross vault model obtained by 3D printing, subjected to failure supports. Numerical simulations allowed quantifying the load-bearing system capacity and describing the structure's different collapse mechanisms; the numerical and experimental results were quite comparable.

Within the framework of the SERA.TA project (Seismology and Earthquake Engineering Research Infrastructure Alliance for Europe), blind prediction and post-diction contests have been organised to assess the numerical approaches' capability to predict and simulate the seismic response of a full-scale masonry cross vault tested at LNEC laboratory (Portugal), in the un-strengthened and strengthened configuration (Blind Prediction Competition, 2023).

The present paper describes the numerical analyses carried out within the framework of the project. The blind prediction analyses were performed before the execution of the shaking table tests; the post-diction analyses were carried out after the experimental tests on a FE model calibrated in the light of the experimental results achieved. The numerical model of the vault has been created by NOSA-ITACA (www.nosaitaca.it/software/), a FE code developed in-house by ISTI-CNR for the analysis and calibration of masonry structures.

The paper is organised as follows.

Section 2 summarizes the main features of the masonry cross vault specimen, describes the FE model developed and the numerical results of the prediction analyses. Section 3 concerns the FE model calibration based on the experimental results. Section 4 shows the results of the post diction numerical analyses performed on the calibrated models. Section 5 summarises the main conclusions of the work.

## 2. Prediction finite element simulations

The groin vault investigated in this paper has been built and tested at the National Laboratory for Civil Engineering (LNEC) in Portugal. The geometry of the mock-up, sketched in Figure 1, is about 3.5x3.5 m in plan and includes: two semi-circular barrel vaults with a net span of 2.9 m, a rise of 0.80 m and a constant thickness of 0.12 m; two masonry piers clamped at the base representing the fixed vault's support; two 0.84x0.84m steel blocks representing the movable supports; three couples of steel rods linking the four abutments. The infill, located on the corners of the vault, is made of bricks, horizontally placed to add weight and stabilize the trusts. (Blind Prediction Competition, 2023).

Preliminary vibration tests have been performed to determine the main natural frequencies and the corresponding mode shapes of the structure. Subsequently, the seismic response of the vault has been investigated by applying in the North-South direction, the accelerogram recorded during the L'Aquila earthquake (reduced by 25%). Once the shaking table test was over, the damaged sample was repaired and an 8 mm reinforcing layer was applied at the vault's extrados. The reinforced vault has been again subjected to dynamic characterization tests to estimate its new dynamic properties and subsequently to the L'Aquila earthquake amplified by 150%.
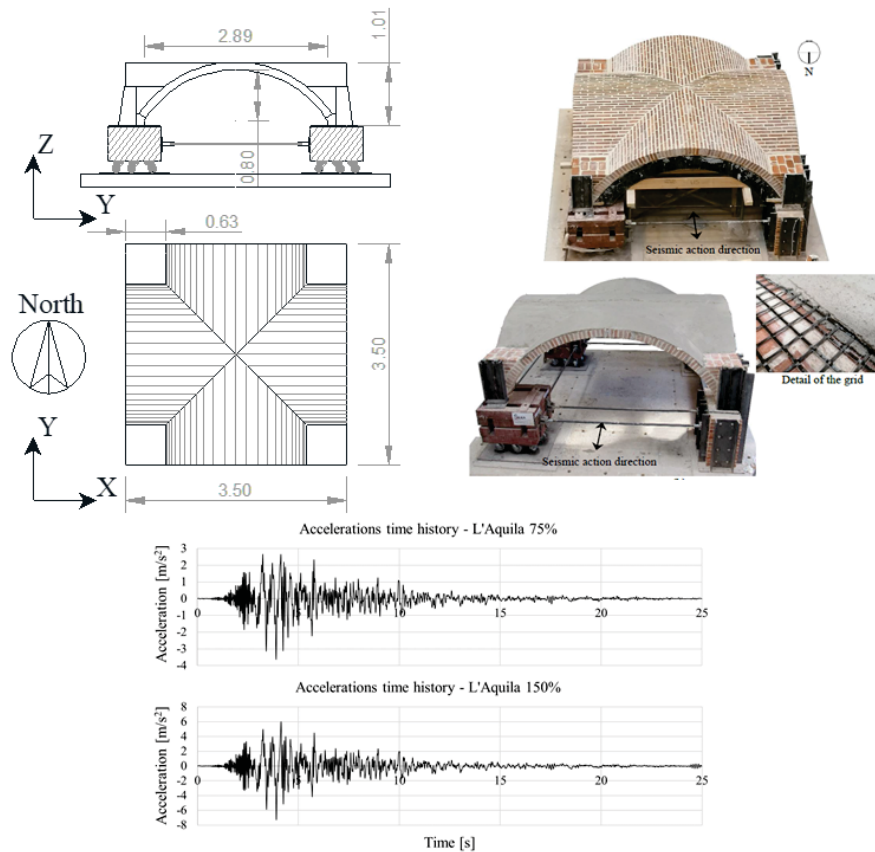
Figure 1 – Dimension of the specimen (length in meters), details of the reinforcement layer and shaking table test input (extracted from Prediction Competition, 2023)

## 2.1. Numerical analyses of the un-strengthened vault

The numerical model of the vault has been created by importing the vault CAD model in the NOSA-ITACA code (www.nosaitaca.it/software/).

NOSA-ITACA is free software developed in-house by ISTI-CNR to disseminate the use of mathematical models and numerical tools in the field of Cultural Heritage. The code is devoted to study the static and dynamic behaviour of masonry structures, and in recent years, it has been updated by adding several features that enable modal analysis, linear perturbation analysis (Girardi et al., 2019a; Pellegrini et al., 2018), and model updating (Girardi et al., 2019b; Girardi et al., 2021).

A detailed finite-element vault model has been created, assuming a macro-modelling approach. The mesh, shown in Figure 2, consists of 83664 4-node isoparametric

tetrahedrons, 7612 8-node isoparametric hexahedrons and six 2-node isoparametric truss elements (element n.25, n.8 and n.35 of the NOSA-ITACA library) with 29353 nodes, for a total of 88056 degrees of freedom. Truss elements are used to model the tie-rods, assuming a cross-section of $8.04 \cdot 10^{-4}$ m$^2$ (corresponding to steel bars of 32 mm diameter). The maximum length of the tetrahedrons' sides is fixed to 4.5 cm to have at least three elements in the vault thickness.

The masonry material constituent the vault has been modelled using the constitutive equation of *masonry-like* (or no-tension) materials that models masonry as an isotropic homogeneous nonlinear elastic material with zero or low tensile strength $\sigma_t$ and infinite or bounded compressive strength $\sigma_c$ (Lucchesi et al., 2008). This equation can consider some of the masonry's peculiarities, including its inability to withstand significant tensile stresses. Assumptions underlying the model are that the infinitesimal strain tensor **E** is the sum of an elastic part **E**$^e$, a fracture part **E**$^f$ and a crushing part **E**$^c$ and that the stress tensor **T**, whose eigenvalues belong to the interval [$\sigma_c$, $\sigma_t$], depends linearly and isotropically on the elastic part of the strain. The fracture and the crushing strain are respectively positive-semidefinite and negative-semidefinite and satisfy suitable orthogonality conditions involving the stress, which turns out to be a nonlinear function of the infinitesimal strain.

The other parts of the mesh (steel blocks, beams, tie-rods, pillars and infill material) are modelled assuming a linear elastic behaviour.

The materials' mechanical properties used in the blind prediction are summarized in Table 1; the masonry's elastic modulus $E$, Poisson ratio $\nu$ and the mass density values, determined on the basis of preliminary experimental tests, are provided to the participants beforehand (Blind Prediction Competition, 2023). Tensile and compressive strengths $\sigma_t$ and $\sigma_c$ are taken equal to 0.0 and 4.55 MPa (the latter obtained as the ratio between the

experimental compressive strength and a partial factor of 2 as suggested by Italian regulations NTC2018). The assumption of zero tensile strength is justified by the fact that this parameter is affected by considerable uncertainty, especially when the complex behaviour of masonry subjected to the combined actions of compression, bending, shear, or torsion is considered (Gonen et al., 2023).

Regarding the boundary conditions, the interaction between the shaking table and the structure is neglected, so the piers and IPE beams are assumed to be clamped at the base (red dots in Figure 2). At the same time, the steel masses are fixed in the vertical direction and movements in the longitudinal and transverse directions (blue dots in Figure 2) are allowed.
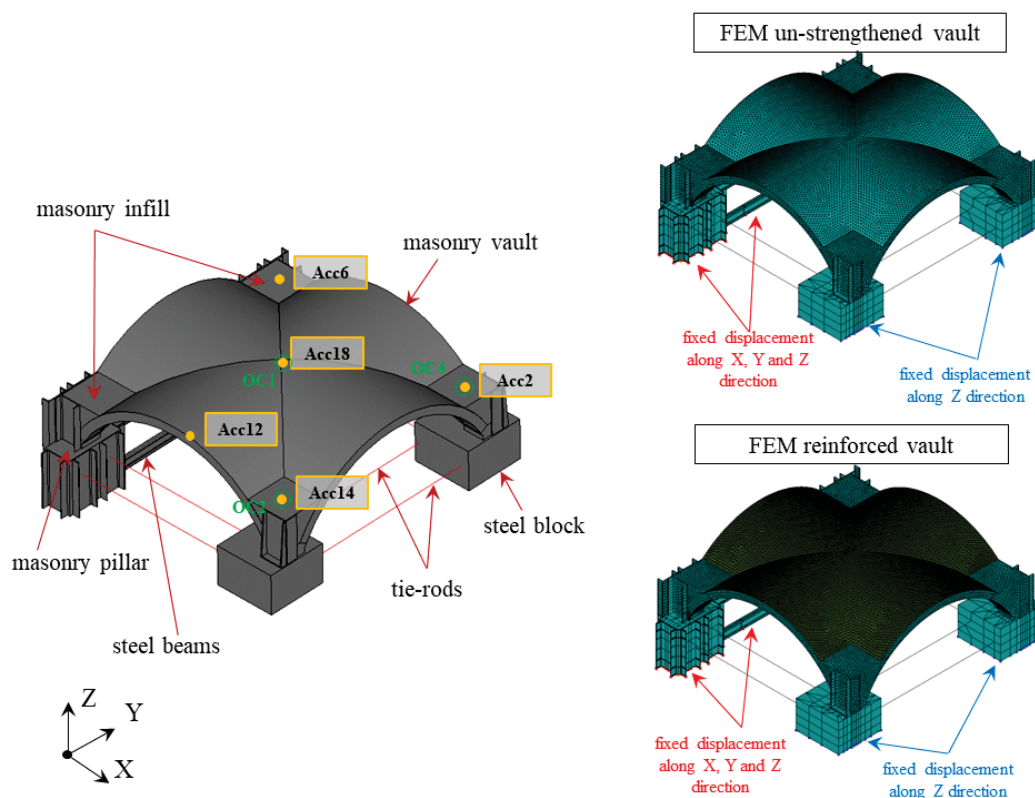


Figure 2 - Vault geometry and finite element model of the un-strengthened (top right) and reinforced cross vault (bottom right).

Table 1 - Mechanical materials properties assumed in prediction phase. $E$, Young's modulus; $\rho$, mass density; $\nu$, Poisson ratio; $\sigma_t$, tensile strength; $\sigma_c$, compressive strength.

| | Masonry vault | Infill and pillars | Steel blocks and beam | Reinforcement |
|---|---|---|---|---|
| $E$ [GPa] | 2.223 | 2.223 | 210.0 | 9.0 |
| $\rho$ [kg/m$^3$] | 2255.2 | 2255.2 | 7880.0 | negligible |
| $\nu$ | 0.2 | 0.2 | 0.3 | 0.2 |
| $\sigma_t$ [MPa] | 0.00 | -- | -- | 0.6 |
| $\sigma_c$ [MPa] | 4.55 | -- | -- | 9.0 |

A preliminary modal analysis has been performed to estimate the dynamic behaviour of the FE model and check the correspondence between experimental and numerical mode shapes. Table 2 reports the experimental $f_{exp}$ (Post-diction Competition, 2023) and numerical frequencies $f_{num}$, the absolute relative error and modal participation factors calculated by NOSA-ITACA. The table shows that the frequencies of the un-strengthened numerical model are higher than the experimental ones, probably due to an unsuitable masonry elastic modulus provided in the blind prediction phase. At the same time, there is a good matching between the numerical and experimental mode shapes (Post-diction Competition, 2023) that are, respectively, a shear mechanism along the Y direction, a bending mode in the X direction and a vertical mode shape along Z, as sketched in Figure 3.
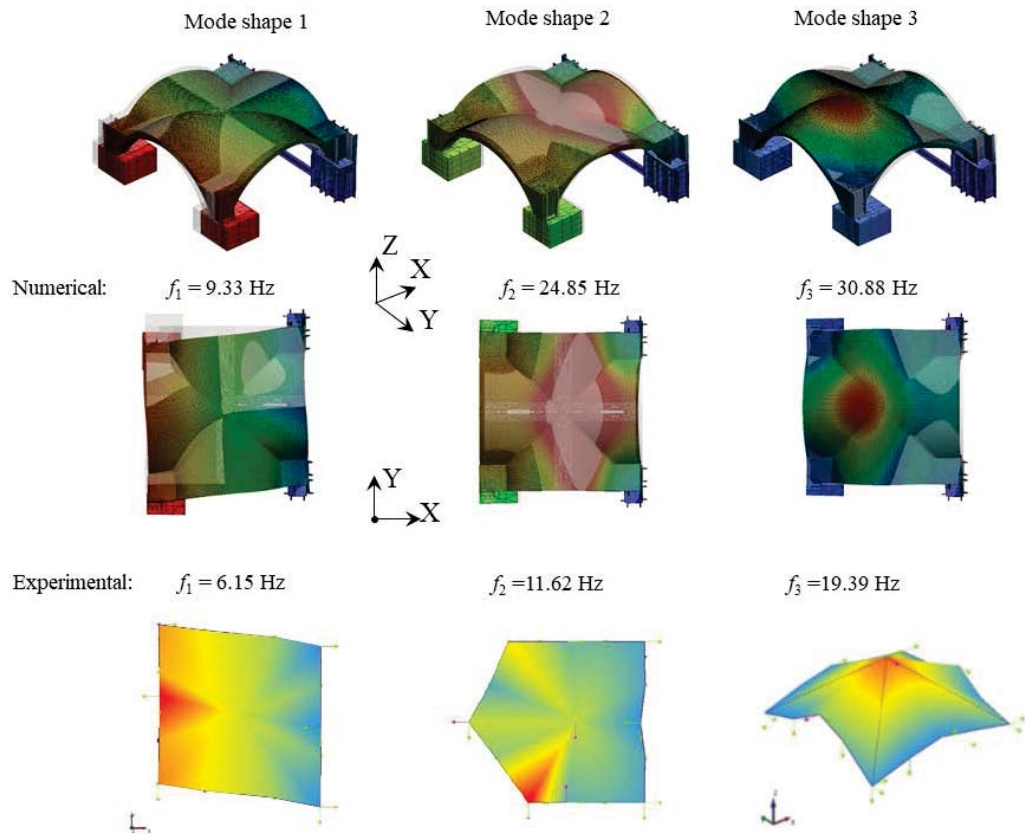
Figure 3 - First three numerical (top) and experimental mode shapes (bottom) (the experimental mode shapes have been extracted from Post-diction Competition, 2023).

Table 2 – Experimental vs numerical frequencies and modal participation factors of the un-strengthened vault.

| | $f_{exp}$ [Hz] | $f_{exp}$ [Hz] | Relative error [%] | Mx [%] | My [%] | Mz [%] |
|---|---|---|---|---|---|---|
| Mode 1 | 6.15 | 9.33 | 51.50 | 0.00 | 73.30 | 0.00 |
| Mode 2 | 11.62 | 24.85 | 113.86 | 63.53 | 0.00 | 0.04 |
| Mode 3 | 19.39 | 30.88 | 59.26 | 0.06 | 0.00 | 0.08 |

Subsequently, a nonlinear dynamic analysis, based on the Newmark integration method (Bathe and Wilson, 1976), has been performed considering the weight of the vault and applying at the base, in the Y direction, the accelerogram recorded during the L'Aquila

earthquake. The analysis has been carried out assuming a time step of 0.0025 s and scaling the accelerogram magnitude by 25%, as indicated by the contest organisers. The damping matrix has been calculated according to the Rayleigh hypothesis (Bathe and Wilson, 1976) with a damping ratio equal to 2.5% (Mendes and Lourenço 2014; Parisse et al. 2021).

In particular, the two Rayleigh coefficients are estimated, considering the first and the twentysecond frequencies, which involve 86% of the mass in the X and Y directions.

The failure mechanism obtained from the nonlinear dynamic analysis is shown in Figure 4. As seen in the picture, it is characterized by a predominant in-plane shear mechanism accompanied, albeit to a lesser extent, by an in-plane bending of the south and north faces arches; the deformation follows the second mode shape of the vault that looks like a typical asymmetrical mode shape of an arch with lateral displacement according to one direction. The deformed shape, sketched in Figure 4 with a deformation scaling factor equal to 20, occurs at the time t = 4.25 s; the contour band refers to the norm of the displacements expressed in meters.
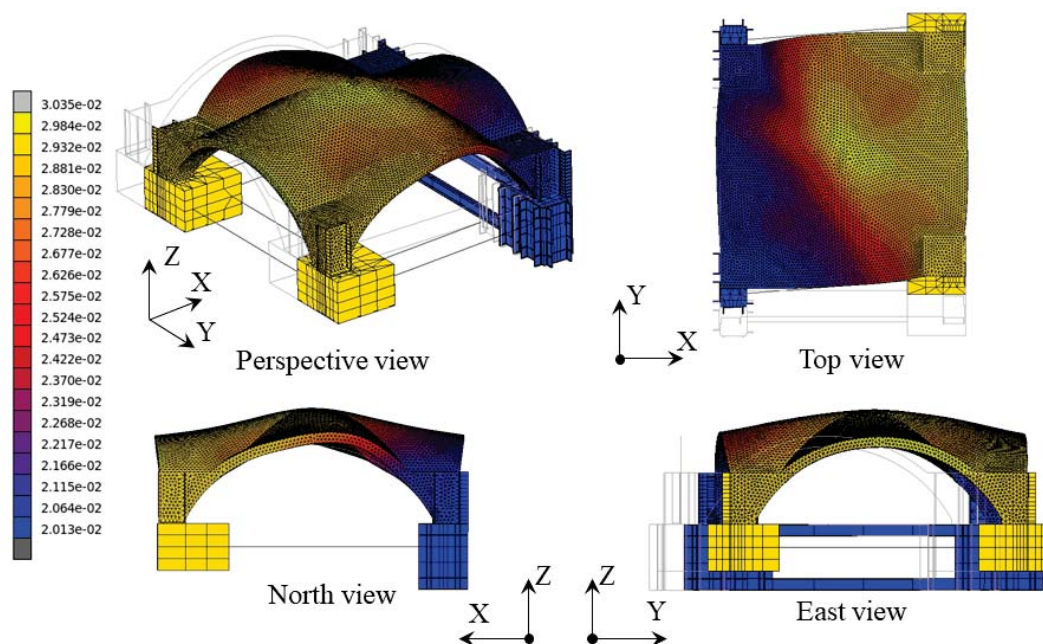


Figure 4 – Deformation shape of the un-strengthened vault at failure.

Figure 5 (up) shows the crack pattern expressed in terms of the norm of the fracture strain tensor $\mathbf{E}^f$, EFEQV; the pattern is characterized by diagonal cracks, with a high concentration of fracture strain at the top of the vault extrados and near the infill. The numerical fracture distribution matches the experimental damage (right side of Figure 5), except for the cracks on the webs that are not visible in the numerical solution. Furthermore, the numerical results show a limited concentration of crushing cracks in small areas near the filling material, as sketched in Figure 5 (bottom).

Table 3 and 4 compare the maximum experimental and numerical total displacements and accelerations of the selected points shown in Figure 2. Regarding displacements, the discrepancy between the results is greater than 90% along the X direction, while in the Y direction it is about 13%, except for $OC_{2-y}$. The numerical model overestimates, in general, the acceleration values in the X and Y directions.
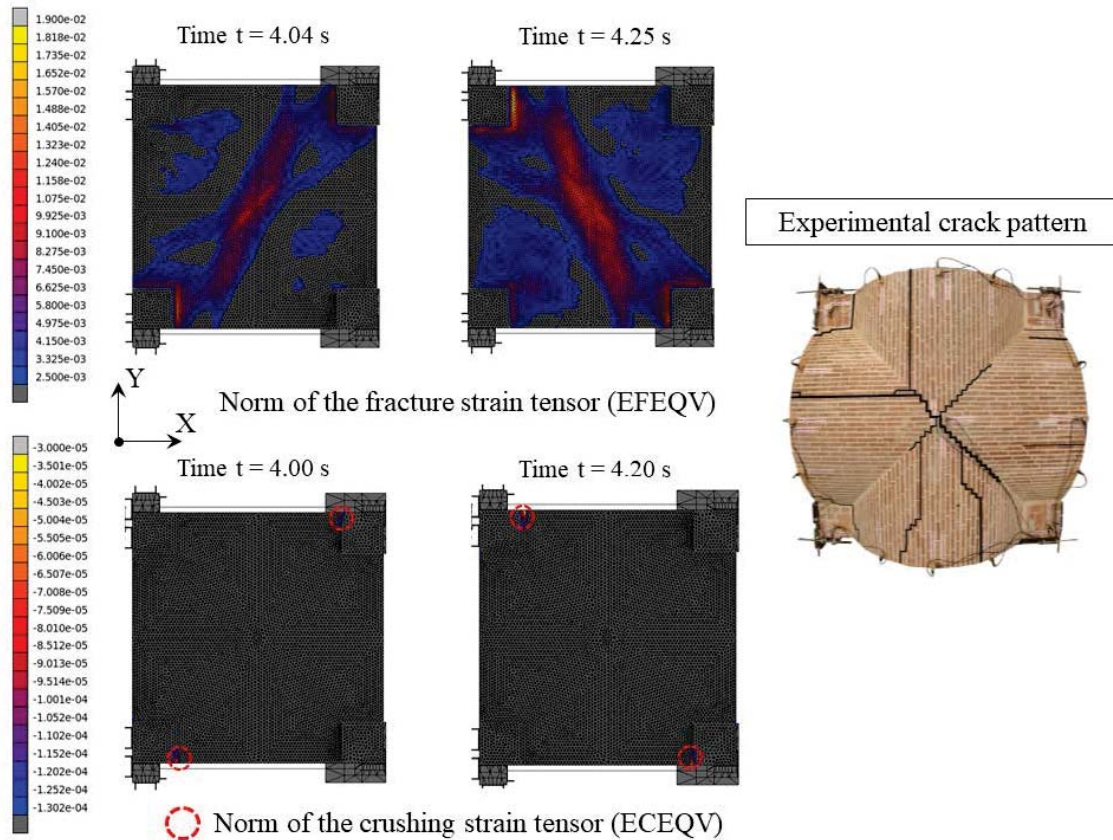
Figure 5 - Crack and crushing pattern of the un-strengthened vault.

Table 3- Maximum total displacements for un-strengthened configuration (absolute value in mm).

| Point | Experimental displacement [mm] | Numerical displacement [mm] | Relative error [%] |
|---|---|---|---|
| $OC_{2-x}$ | 4.01 | 0.29 | 92.77 |
| $OC_{4-x}$ | 7.78 | 0.24 | 96.92 |
| \|Average\| | -- | -- | 94.85 |
| $OC_{1-y}$ | 27.90 | 31.39 | -12.51 |
| $OC_{2-y}$ | 70.66 | 31.40 | 55.56 |
| $OC_{4-y}$ | 35.83 | 31.37 | 12.45 |
| \|Average\| | -- | -- | 26.84 |

Table 4 - Maximum total acceleration for un-strengthened configuration (absolute value in m/s$^2$).

| Point | Experimental acceleration [m/s$^2$] | Numerical acceleration [m/s$^2$] | Relative error [%] |
|---|---|---|---|
| Acc$_{2-x}$ | 4.39 | 8.56 | -94.99 |
| Acc$_{6-x}$ | 3.98 | 4.63 | -16.33 |
| Acc$_{12-x}$ | 3.44 | 4.88 | -41.86 |
| Acc$_{14-x}$ | 5.23 | 9.55 | -82.60 |
| Acc$_{18-x}$ | 3.77 | 5.03 | -33.42 |
| \|Average\| | -- | -- | 53.80 |
| Acc$_{2-y}$ | 4.53 | 5.66 | -24.94 |
| Acc$_{6-y}$ | 4.51 | 4.90 | -8.65 |
| Acc$_{12-y}$ | 4.92 | 8.89 | -80.69 |
| Acc$_{14-y}$ | 4.44 | 6.43 | -44.82 |
| Acc$_{18-y}$ | 3.44 | 6.11 | -77.62 |
| \|Average\| | -- | -- | 47.34 |

The analysis of the previous figures and tables allows one to make the following remarks:

- Young's modulus employed must be updated to fit the natural frequencies of the un-strengthened vault;

- the boundary conditions assigned to the model are suitable to reproduce the mode shapes of the specimen;

- the compressive strength does not influence the nonlinear dynamic numerical results;

- the hypothesis of the masonry vault's zero tensile strength allows predicting the crack pattern due to the seismic action applied to the structure.

## 2.2. Nonlinear dynamic analysis of the reinforced vault

The FE model used to perform the numerical analysis of the un-strengthened vault has been modified to simulate the presence of the reinforcement. For this purpose, 12732 8-node collapsed hexahedron elements have been added at the extrados of the original model creating a continuous layer 8 mm thick. The new model consists of 101014 elements and 35883 nodes for a total number of 107649 degrees of freedom; a 5.6 maximum aspect ratio characterises the mesh, still considered acceptable from the point of view of the quality of the results.

The reinforcement layer, as the masonry vault, is modelled by the constitutive equation of no-tension materials, assuming the Young's modulus $E = 9$ GPa, Poisson ratio $v = 0.2$, tensile strength $\sigma_t = 0.6$ MPa, compressive strength $\sigma_c = 9.0$ MPa and neglecting the mass density.

The tensile and compressive strength are recovered considering the debonding and the compressive strength of the Kerakoll mortar employed to form the reinforcement layer, divided by a partial factor equal to 1.67, as suggested by the Italian Guidelines CNR-DT-215-2018.

The assumptions made for the un-strengthened vault still apply to the remaining mesh parts.

As in subsection 2.1, a nonlinear dynamic analysis has been performed with a time step of 0.0025 s and applying, in the Y direction, the accelerogram recorded during the L'Aquila earthquake amplified by 150% (as indicated by the contest organisers). The damping matrix has still been calculated according to the Rayleigh hypothesis with a damping ratio of 2.5%.

Again, the dynamic analysis results suggest that the failure mechanism is an in-plane shear mechanism coupled with an in-plane bending of the south and north faces arches;

the crack pattern, shown in Figure 6, is in agreement with the experimental one showing damage above the fixed piers, diagonal cracks and opening of the vault close to the level of the springing. The numerical results does not exhibit horizontal cracks at the base of the supports or fractures on the infill in the southwest corner. Furthermore, Figure 6 shows a limited concentration of crushing cracks in small areas near the filling material.
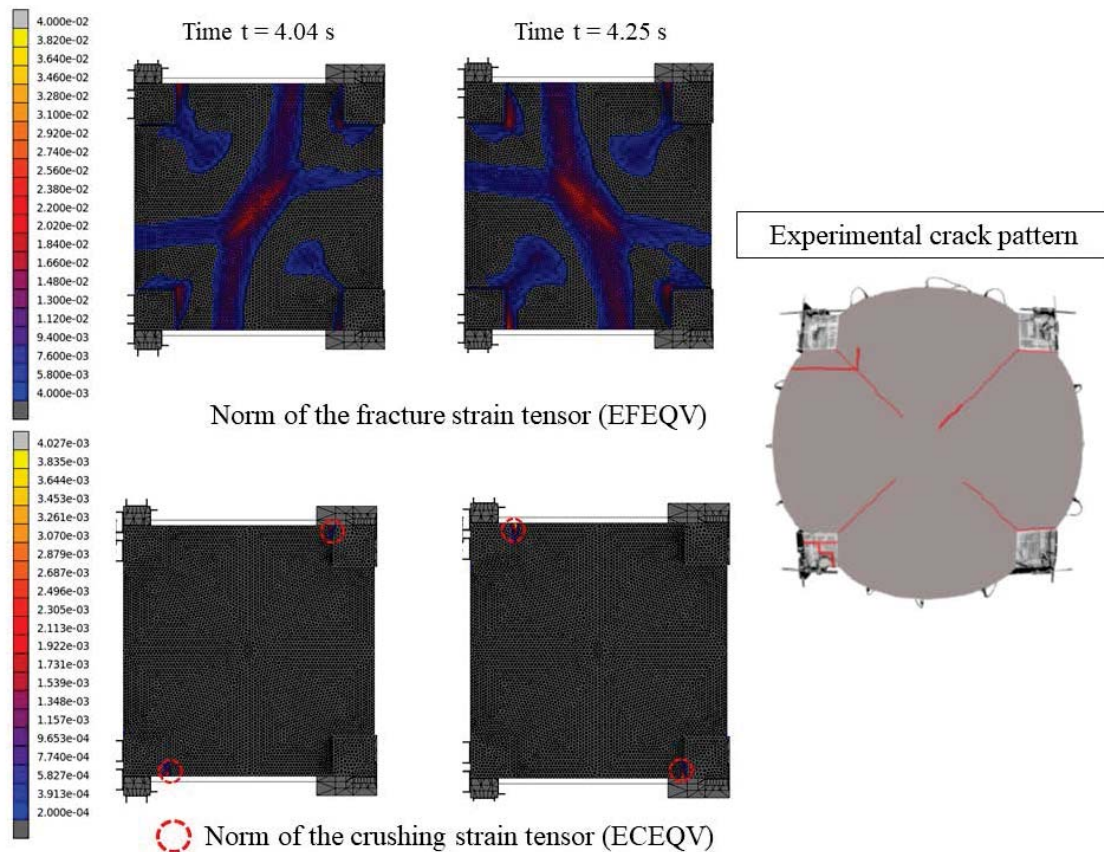


Figure 6 - Crack and crushing pattern of the strengthened vault.

Table 5 and Table 6 compare the maximum experimental and numerical total displacements and accelerations of the selected points shown in Figure 2. Again, the numerical model overestimates the displacements in the X and Y directions. The predicted value of the acceleration in the X direction is affected by an average relative error of 29%, the average relative error in the Y direction is 20%.

Table 5 - Maximum total displacements for reinforced configuration (absolute value in mm).

| Point | Experimental displacement [mm] | Numerical displacement [mm] | Relative error [%] |
|---|---|---|---|
| $OC_{2-x}$ | 42.8 | 0.76 | 98.22 |
| $OC_{4-x}$ | 12.77 | 0.43 | 96.63 |
| \|Average\| | -- | -- | 97.43 |
| $OC_{1-y}$ | 56.03 | 60.21 | -7.46 |
| $OC_{2-y}$ | 63.47 | 53.63 | 15.50 |
| $OC_{4-y}$ | 62.17 | 53.17 | 14.48 |
| \|Average\| | -- | -- | 12.48 |

Table 6 - Maximum total acceleration for reinforced configuration (absolute value in $m/s^2$).

| Point | Experimental acceleration [$m/s^2$] | Numerical acceleration [$m/s^2$] | Relative error [%] |
|---|---|---|---|
| $Acc_{2-x}$ | 10.03 | 5.80 | 42.17 |
| $Acc_{6-x}$ | 11.73 | 10.75 | 8.35 |
| $Acc_{12-x}$ | 9.47 | 7.97 | 15.84 |
| $Acc_{14-x}$ | 17.33 | 9.89 | 42.93 |
| $Acc_{18-x}$ | 8.17 | 5.53 | 32.31 |
| \|Average\| | -- | -- | 28.32 |
| $Acc_{2-y}$ | 9.41 | 8.15 | 13.39 |
| $Acc_{6-y}$ | 9.06 | 9.71 | -7.17 |
| $Acc_{12-y}$ | 8.37 | 10.50 | -25.45 |
| $Acc_{14-y}$ | 10.56 | 8.25 | 21.88 |
| $Acc_{18-y}$ | 7.67 | 10.08 | -31.42 |
| \|Average\| | -- | -- | 19.86 |

Some comments follow from the results summarized in the previous pictures and tables:

- the constitutive equation of *masonry-like* materials seems to be able to simulate the reinforcement behaviour;

- the partial factor used to reduce the tensile strength, could has affected the reinforcement response given the presence of severe diagonal cracks;

- here, too, the compressive strength of the vault and reinforcement does not influence the results of the dynamic analyses.

## 3. Finite element models calibration

Based on the prediction numerical analyses and experimental tests, the FE models described in Section 2 have been calibrated to catch the mock-up's dynamic properties and reproduce its seismic response.

Starting with the un-strengthened vault case, the model updating has been performed by exploiting the linear perturbation analysis (LPA) (Pellegrini et al., 2018) under the following assumptions: i) null tensile strength for the masonry vault; ii) infinite compressive strength for vault and infill; iii) infill modelled by the no-tension materials constitutive equation assuming a tensile strength equal to 0.31 MPa.

The last assumption derives from the observation that one of the fillings gets damaged in the reinforced structure; thus, the hypothesis of linear elastic material, assumed in the prediction phase, seems unsuitable. The application of LPA is justified by the assumption that the vault has zero tensile strength, which makes it possible the formation of micro-cracks due to the structure's weight.

The linear perturbation analysis consists in solving the following constrained generalized eigenvalue problem:

$$K_T \phi = \omega^2 M \phi$$

where $K_T$ and $M \in \mathbb{R}^{n \times n}$ are the tangent stiffness and mass matrices of the finite-element model with $n$ degrees of freedom, $\phi \in \mathbb{R}^n$ is the eigenvector (mode shape) associated with the corresponding eigenvalue $\omega^2$ (the corresponding natural frequency of the system is $f = \omega/2\pi$). The matrix $K_T$, used in place of the elastic stiffness matrix, is calculated using the solution to the equilibrium problem of the structure subjected to static loads, considering, therefore, the possible presence of cracks in the body.

To match the experimental frequencies of the vault reported in Table 2 and the corresponding mode shapes, LPA has been applied iteratively, varying the Young's modulus of the vault, infill and pillars until finding an optimal value that minimizes the discrepancy between experimental and numerical frequencies.

Table 7 summarizes the results in terms of numerical frequencies $f_{LPA}$ corresponding to the optimal Young's modulus value $E_{opt}$, their relative error $\Delta f_{LPA}$ with respect to the experimental counterparts' $f_{exp}$ and the MAC value (Brinker & Ventura, 2015) calculated between the numerical and experimental mode shapes.

For the sake of comparison, Table 7 reports the same quantities obtained by applying a standard model updating (SMU) (Girardi et al., 2021). The analysis of the results shows that the two solutions are very close to each other, even if the solution obtained with LPA seems to better approximate the dynamic behaviour of the vault. Furthermore, both models are too stiff in the X direction, resulting in overestimating the second frequency.

Table 7 – Comparison between the experimental and numerical dynamic properties

| Mode | $f_{exp}$ [Hz] | $f_{LPA}$ [Hz] | $\Delta f_{LPA}$ [%] | $MAC_{LPA}$ | $f_{SMU}$ [Hz] | $\Delta f_{SMU}$ [%] | $MAC_{SMU}$ |
|---|---|---|---|---|---|---|---|
| 1 | 6.15 | 6.15 | 0.00 | 0.92 | 6.15 | 0.00 | 0.92 |
| 2 | 11.62 | 18.29 | -57.40 | 0.18 | 18.65 | -60.50 | 0.21 |

| | | | | | | | |
|---|---|---|---|---|---|---|---|
| 3 | 19.39 | 20.02 | -3.25 | 0.71 | 20.74 | -6.96 | 0.67 |
| | | $E_{opt}$ = 0.8440 GPa | | | $E_{opt}$ = 0.7945 GPa | | |

It is emphasized that assuming an isotropic behaviour of the vault, the only way to match the second frequency would be to modify the system stiffness in the X direction through a fictitious reduction of the elastic modulus of the tie-rods parallel to this direction. Therefore, considering the masonry and tie-rods Young's moduli as parameters to be optimized, the results reported in Table 8 is obtained.

Table 8 - Comparison between experimental and numerical dynamic properties in case of elastic modulus reduction of the tie-rods along X direction.

| Mode | $f_{exp}$ [Hz] | $f_{LPA}$ [Hz] | $\Delta f$ [%] | MAC | $f_{MU}$ [Hz] | $\Delta f$ [%] | MAC |
|---|---|---|---|---|---|---|---|
| 1 | 6.15 | 6.15 | 0.00 | 0.86 | 6.15 | 0.00 | 0.86 |
| 2 | 11.62 | 11.12 | 0.00 | 0.46 | 11.62 | 0.00 | 0.53 |
| 3 | 19.39 | 26.16 | 34.91 | 0.78 | 25.67 | 32.39 | 0.65 |
| | masonry | $E_{opt}$ = 1.315 GPa | | | $E_{opt}$ = 1.051 GPa | | |
| | steel | $E_{opt}$ = 30.825 GPa | | | $E_{opt}$ = 30.825 GPa | | |

However, this solution is not feasible since the load cells placed on the steel bars during experimental dynamic tests have not shown any stress variation. Therefore, for the subsequent analyses, the model having only the masonry Young's modulus obtained through an LPA will be employed.

As far as the reinforced model is concerned, its calibration has been done starting from the un-strengthened model, assuming that after the seismic shock, the specimen is perfectly repaired and the initial mechanical characteristics are entirely recovered. Therefore, the only parameter to be optimized is the reinforcement Young's modulus.

The estimated value through a LPA, based on the experimental frequencies of the repaired model, is around 0.7 GPa. The other reinforcement properties employed in post-diction analyses and recovered by the Kerakoll mortar datasheets are mass density 2000 kg/m³ and tensile strength 1MPa.

## 4. Post-diction: analysis and results

As in the prediction phase, two nonlinear dynamic analyses have been executed employing the calibrated numerical models described in Section 3. The accelerogram recorded during the L'Aquila earthquake is applied at the model's base, in the Y direction, with a reduction of 25% in the un-strengthened model, and an amplification of 150% in the reinforced one; the time step for both simulations is 0.0025 s. In each analysis the viscous damping matrix has been calculated for a damping ratio of 2.5% and the two coefficients are estimated, considering again the first and twenty-second frequencies, which engage 86% of the mass in the X and Y directions.

The post-diction results are here investigated in terms of crack pattern, Figure 7-Figure 9 (un-strengthened model) and Figure 12-Figure 15 (reinforced model); displacements and accelerations time histories Figure 10, Figure 11 (un-strengthened model) and Figure 16, Figure 17 (reinforced model), as well as the maximum absolute values of displacements and accelerations (Table 9-Table 10 and Table 11-Table 12 for un-strengthened and reinforced case respectively) of the selected points reported in Figure 2.

As regards the un-strengthened case, in the light of the results summarized in the following figures and tables, it is possible to state that:

- as in the prediction stage, the numerical pattern matches well the vault fractures even with a trace of the crack in the webs (Figure 7). The damage along the two diagonals arises at different times, due to the hypothesis of elasticity, although nonlinear, assumed to model the masonry of the vault;

- fracture concentrations are present near to infill and in the face arches, as it happens in the experimental specimen and shown in Figure 8 and Figure 9;

- the numerical displacement time histories of the points $OC_1$ and $OC_4$ along the Y direction agree with the experimental results, suggesting a reasonable estimation of the damping parameters. Furthermore, their maximum values occur at the same time;

- the numerical values of the displacement in the X direction are underestimated with respect to the experimental ones (Table 9);

- the absolute value of the average relative error made in estimating the maximum X and Y displacements decreases from 94.85% and 26.84% (Table 3) for the prediction analyses to 88.29% and 22.44% (Table 9) for the post-diction;

- the numerical acceleration time histories, along Y, of the selected points fit well with the experimental counterparts, starting from the time t =2 s, while in the previous time interval, their value is underestimated (Figure 11);

- the value of the predicted accelerations in the X direction is higher than the measured values (Table 10);

- the absolute value of the average relative error in estimating the maximum X and Y accelerations decreases from 53.80% and 47.34% (Table 3, prediction analysis) to 31.12% and 8.57% (Table 9 post-diction simulation).
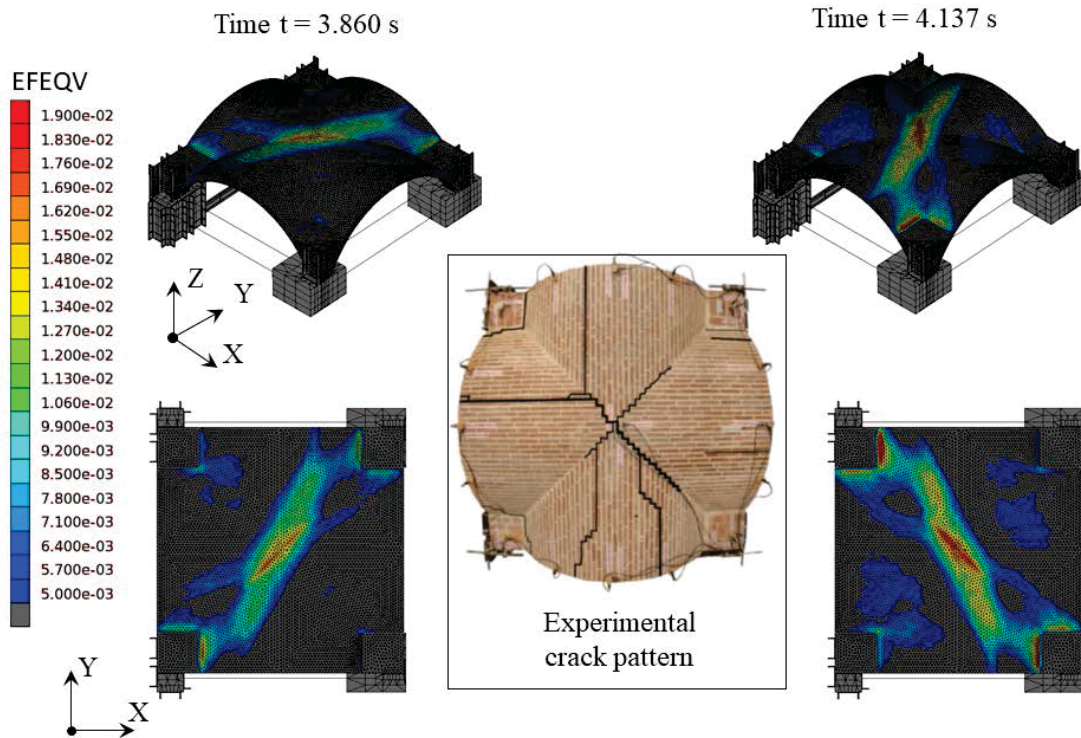
Figure 7- Crack pattern of the un-strengthened vault in the post-diction: perspective (up) and top view (bottom).
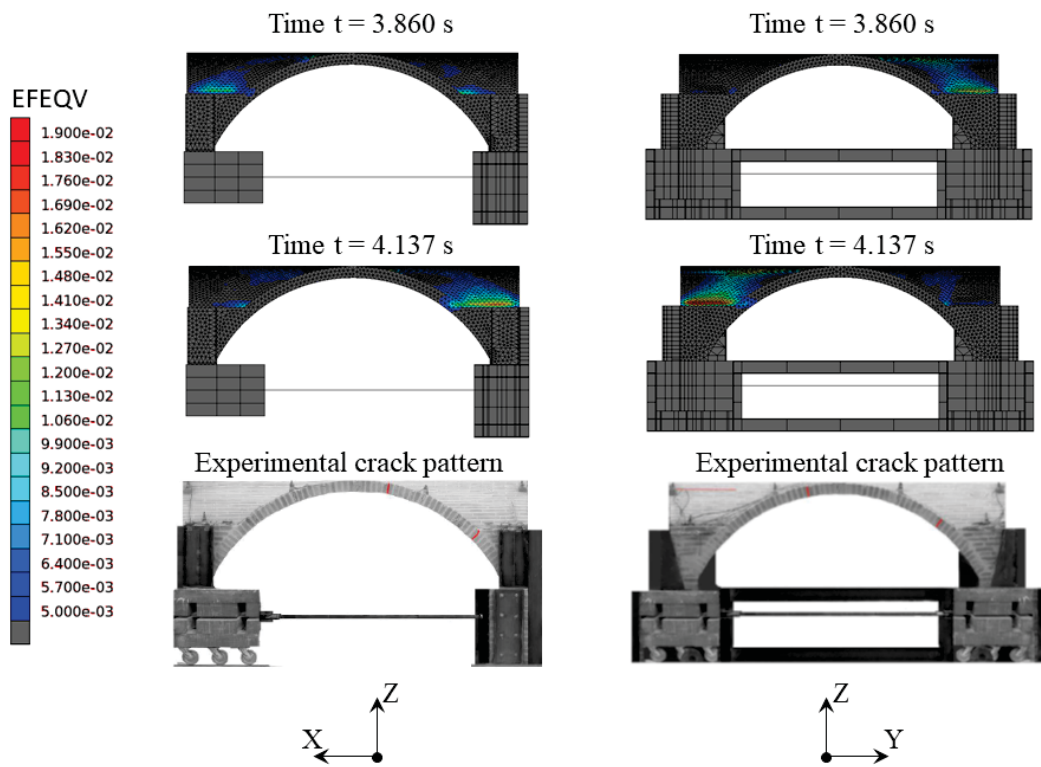
Figure 8 - Crack pattern of the un-strengthened vault in the post-diction: north (left) and east (right) view.
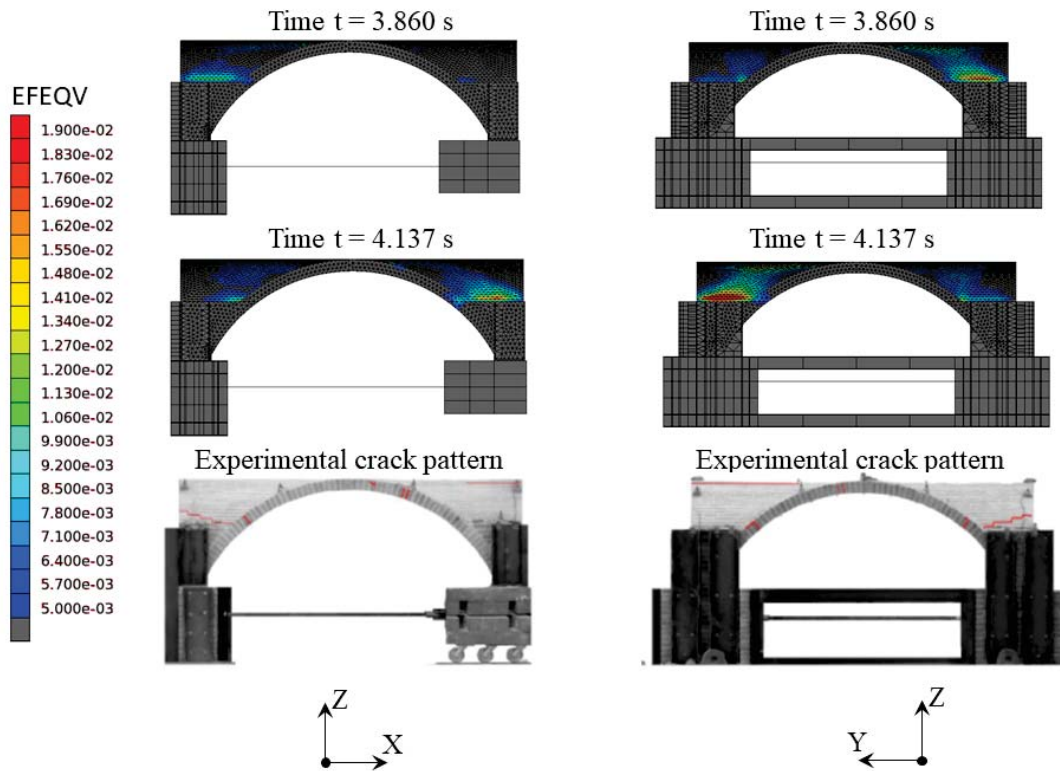
Figure 9 - Crack pattern of the un-strengthened vault in the post-diction: south (left) and west (right) view.
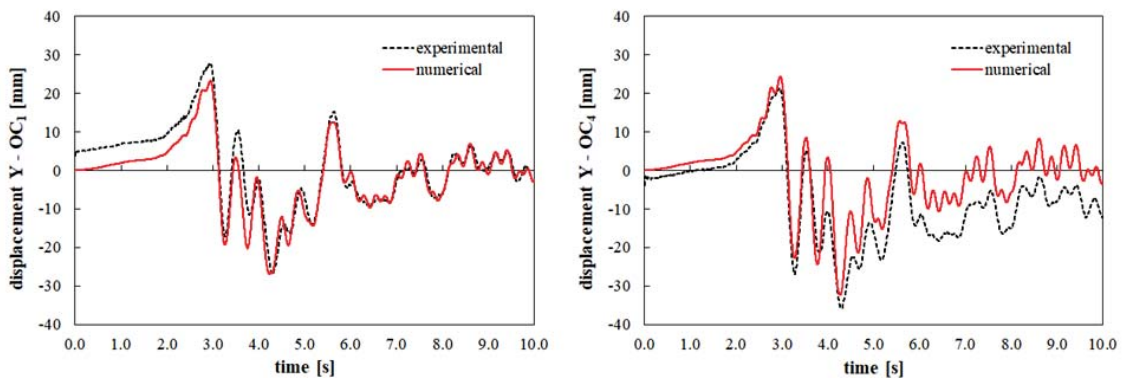


Figure 10 – Displacement time history of $OC_1$ (left) and $OC_4$ (right) points, un-strengthened model: experimental results (dashed black line) versus numerical one (continuous red line).
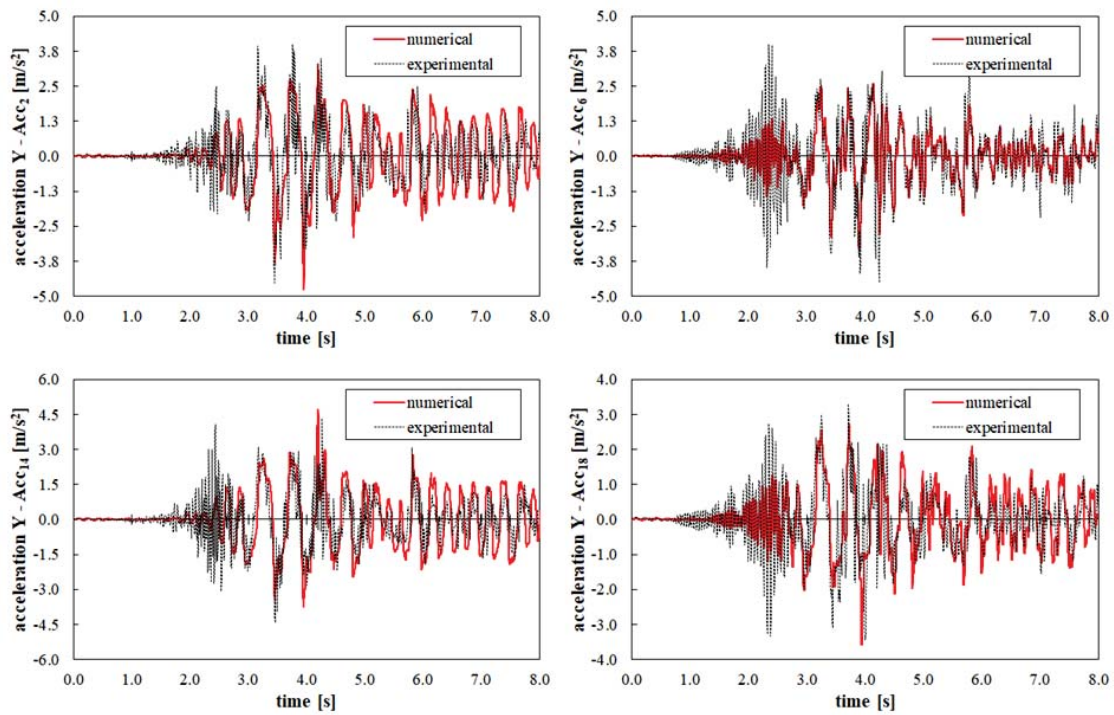
Figure 11- Acceleration time history of $Acc_2$, $Acc_6$, $Acc_{14}$ and $Acc_{18}$ points, un-strengthened model: experimental results (dashed black line) versus numerical one (continuous red line).

Table 9- Maximum total displacements for un-strengthened configuration (absolute value in mm).

| Point | Experimental displacement [mm] | Numerical displacement [mm] | Relative error [%] |
|---|---|---|---|
| $OC_{2-x}$ | 4.01 | 0.62 | 84.54 |
| $OC_{4-x}$ | 7.78 | 0.62 | 92.03 |
| \|Average\| | -- | -- | 88.29 |
| $OC_{1-y}$ | 27.90 | 26.95 | 3.41 |
| $OC_{2-y}$ | 70.66 | 32.26 | 54.34 |
| $OC_{4-y}$ | 35.83 | 32.40 | 9.57 |

| | | | 22.44 |
|---|---|---|---|
| |Average| | -- | -- | 22.44 |

Table 10 - Maximum total acceleration for un-strengthened configuration (absolute value in m/s$^2$).

| Point | Experimental acceleration [m/s$^2$] | Numerical acceleration [m/s$^2$] | Relative error [%] |
|---|---|---|---|
| Acc$_{2\text{-}x}$ | 4.39 | 5.06 | -15.26 |
| Acc$_{6\text{-}x}$ | 3.98 | 6.06 | -52.26 |
| Acc$_{12\text{-}x}$ | 3.44 | 4.70 | -36.62 |
| Acc$_{14\text{-}x}$ | 5.23 | 4.66 | 10.90 |
| Acc$_{18\text{-}x}$ | 3.77 | 2.24 | 40.58 |
| |Average| | -- | -- | 31.12 |
| Acc$_{2\text{-}y}$ | 4.53 | 4.74 | -4.64 |
| Acc$_{6\text{-}y}$ | 4.51 | 3.30 | 26.83 |
| Acc$_{12\text{-}y}$ | 4.92 | 4.87 | 1.02 |
| Acc$_{14\text{-}y}$ | 4.44 | 4.72 | -6.31 |
| Acc$_{18\text{-}y}$ | 3.44 | 3.58 | -4.07 |
| |Average| | -- | -- | 8.57 |

As far as the reinforced FE model is concerned, the following conclusions can be drawn from the analysis of numerical results:

- the numerical crack pattern shows damaged areas near the infill and at the top of the vault but not along the two diagonal (Figure 12); this mismatch is probably caused by an excessive tensile strength assumed for the reinforcement. Figure 13 instead reveals a numerical crack pattern of the vault extrados (underlying the reinforcement layer) similar to the experimental one detected on the reinforcement itself;

- Figure 14 and Figure 15 highlight a good correspondence between numerical and

experimental crack pattern of the four face arches;

- the horizontal crack at the base of the pillar is missing because of the assumed boundary conditions that neglect the interaction with the shaking table (Figure 14);

- the numerical displacement time histories of $OC_1$ and $OC_4$ points, along the Y direction, fit very well the experimental results (Figure 16);

- the numerical values of the displacement in the X direction are underestimated with respect to the experimental ones (Table 11);

- the numerical acceleration time histories, along Y, of the points $Acc_2$ and $Acc_{14}$ agree with the experimental counterparts, while those related to $Acc_6$ and $Acc_{18}$ match starting from three seconds (Figure 17);

- the absolute value of the average relative error in Y accelerations drops from 19.86% (Table 6, prediction analysis) to 10.20% (Table 12 post-diction analysis).
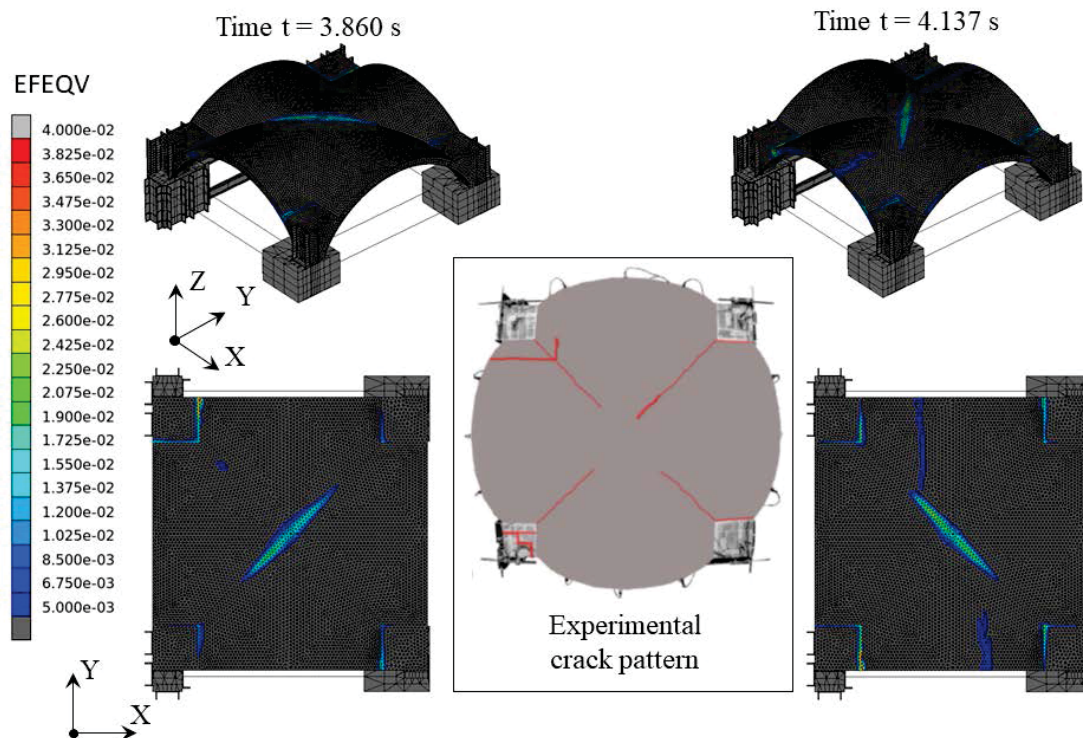


Figure 12 - Crack pattern of the reinforced vault in the post-diction analysis: perspective (up) and top view (bottom).
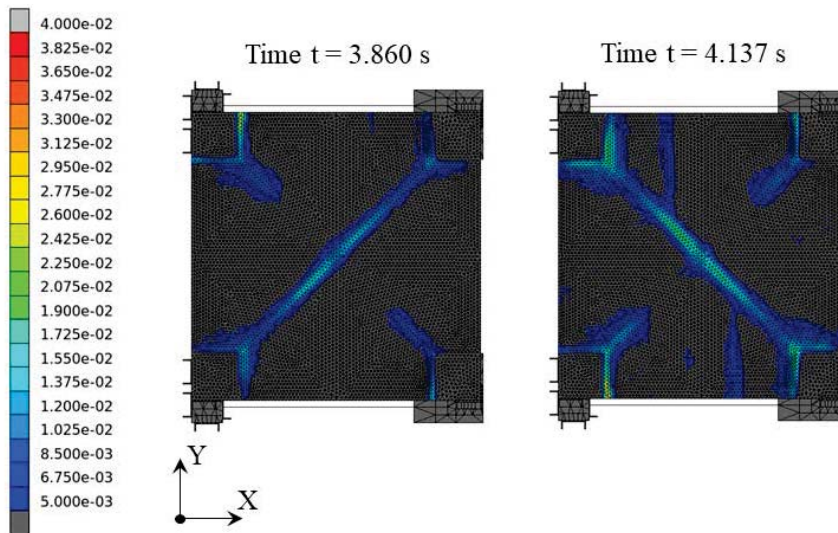
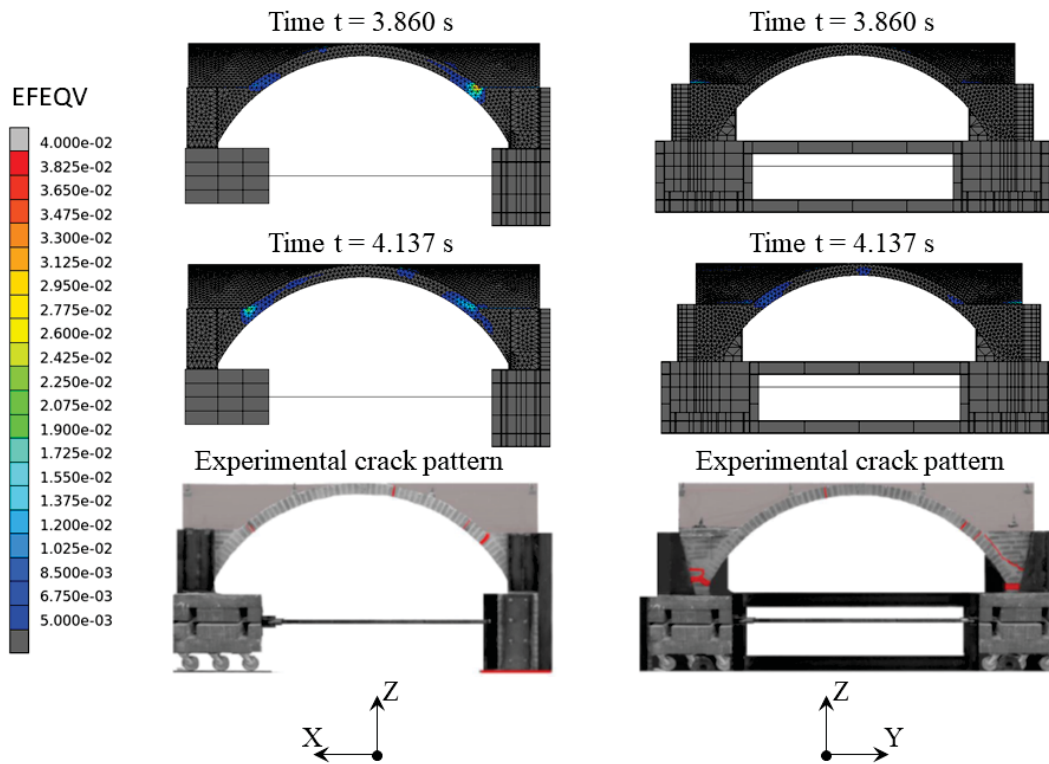Figure 13 - Crack pattern of the vault extrados in the post-diction analysis.



Figure 14 - Crack pattern of the reinforced vault in the post-diction analysis: north (left) and east (right) view.
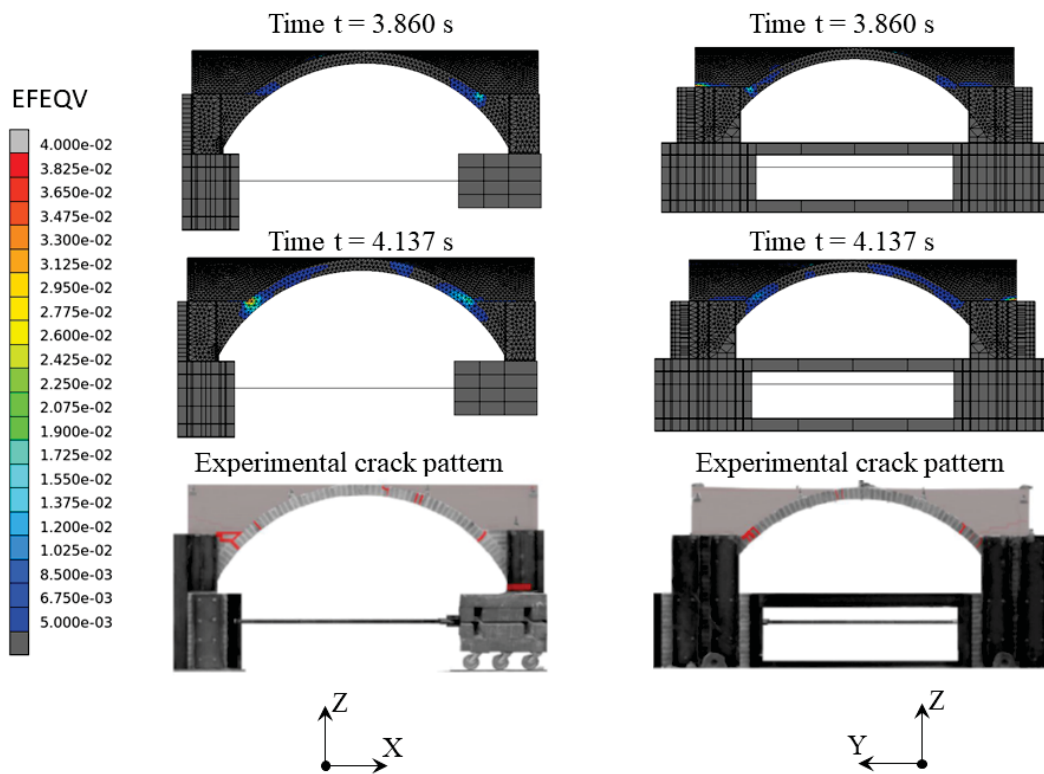
Figure 15 - Crack pattern of the reinforced vault in the post-diction analysis: south (left) and west (right) view.
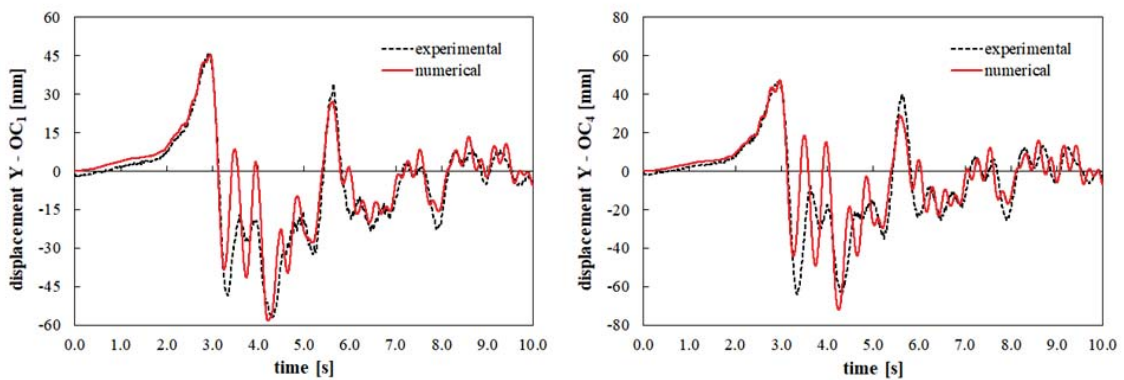


Figure 16 - Displacement time history of $OC_1$ (left) and $OC_4$ (right) points, reinforced model: experimental results (dashed black line) versus numerical one (continuous red).
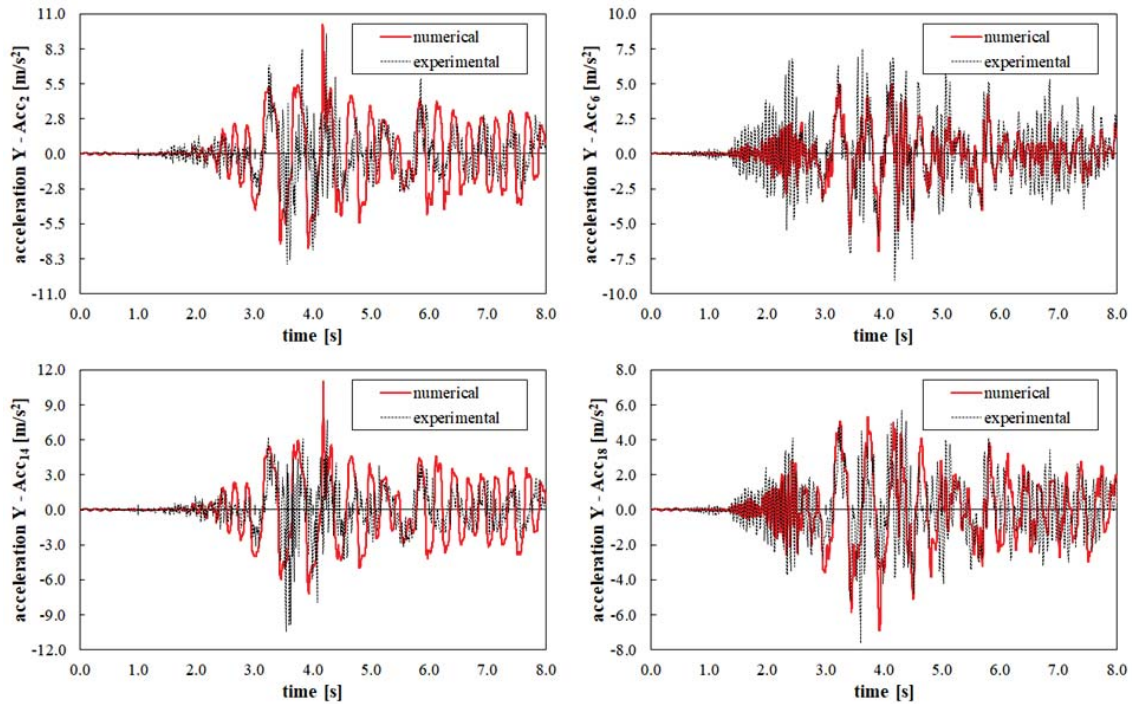
Figure 17 - Acceleration time history of $Acc_2$, $Acc_6$, $Acc_{14}$ and $Acc_{18}$ points, reinforced model: experimental results (dashed black line) versus numerical one (continuous red).

Table 11 - Maximum total displacements for reinforced configuration (absolute value in mm).

| Point | Experimental displacement [mm] | Numerical displacement [mm] | Relative error [%] |
|---|---|---|---|
| $OC_{2-x}$ | 42.8 | 1.65 | 96.14 |
| $OC_{4-x}$ | 12.77 | 0.89 | 93.03 |
| \|Average\| | -- | -- | 94.59 |
| $OC_{1-y}$ | 56.03 | 58.20 | -3.87 |
| $OC_{2-y}$ | 63.47 | 72.20 | -13.75 |
| $OC_{4-y}$ | 62.17 | 71.90 | -15.65 |
| \|Average\| | -- | -- | 11.09 |

Table 12 - Maximum total acceleration for reinforced configuration (absolute value in m/s$^2$).

| Point | Experimental acceleration [m/s$^2$] | Numerical acceleration [m/s$^2$] | Relative error [%] |
|---|---|---|---|
| Acc$_{2-x}$ | 10.03 | 15.40 | -53.54 |
| Acc$_{6-x}$ | 11.73 | 7.10 | 39.47 |
| Acc$_{12-x}$ | 9.47 | 10.60 | -11.93 |
| Acc$_{14-x}$ | 17.33 | 5.85 | 66.24 |
| Acc$_{18-x}$ | 8.17 | 7.03 | 13.95 |
| |Average| | -- | -- | 37.03 |
| Acc$_{2-y}$ | 9.41 | 10.10 | -7.33 |
| Acc$_{6-y}$ | 9.06 | 6.90 | -23.84 |
| Acc$_{12-y}$ | 8.37 | 8.82 | -5.38 |
| Acc$_{14-y}$ | 10.56 | 10.90 | -3.22 |
| Acc$_{18-y}$ | 7.67 | 6.81 | 11.21 |
| |Average| | -- | -- | 10.20 |

## 5. Conclusion

The paper describes the outcomes of numerical analyses conducted under the pre and post-diction contest organised within the framework of the SERA.TA project (Seismology and Earthquake Engineering Research Infrastructure Alliance for Europe). The seismic response of a 1:1 masonry cross vault specimen realised and tested at the LNEC laboratory, considering its un-strengthened and reinforced configurations, has been simulated by the NOSA-ITACA code, a non-commercial software developed by ISTI-CNR.

Two refined finite-element models of the vault have been created, for the un-strengthened and reinforced case, modelling the masonry vault as a no-tension material with zero

tensile strength and the reinforcement as a *masonry-like* material with limited tensile strength. The modal and nonlinear dynamic analyses carried out in the prediction phase have highlighted, in both cases: i) the ability of the *masonry-like* model to predict the damaged area during the seismic shock; ii) the suitability of the boundary conditions to reproduce the specimen dynamic response in terms of mode shapes; iii) the need to consider a reduced Young's modulus, compared to the experimental one, in order to reproduce the dynamic vault behaviour in terms of frequencies; iv) the possibility to model the reinforcement via the constitutive equation of no tension materials.

In the post-diction phase, the FE models were calibrated using a linear perturbation analysis based on the experimental dynamic properties.

Then nonlinear dynamic analyses were carried out, assigning scaled real accelerograms at the meshes base. The numerical results have been compared to the experimental ones in terms of crack pattern, failure mechanism, maximum total displacements and accelerations at selected points.

As far as the un-strengthened model is concerned, the crack pattern fits well with the experimental damage even if the fractures along the specimen diagonals do not form simultaneously. The numerical displacement and acceleration time histories along the direction of the seismic action agree with the experimental results, while in the orthogonal direction, there is a misalignment. Relating to the strengthened case, the match between the experimental and numerical crack pattern on the reinforcement layer is not better than the one obtained in the prediction phase, while the one on the façade arches is improved. Fractures at the infill supports are missing. The numerical displacement time histories in the Y direction catch the seismic response of the specimens in a good way; however, the global analysis of the results shows that the model employed to simulate the behaviour of the reinforcement needs to be further investigated and improved.

## Acknowledgements

## Reference

Alforno, M., Venuti, F., Monaco, A., & Calderini, C. (2022). "Seismic behaviour of cross vaults with different brick pattern". *Bulletin of Earthquake Engineering*, 1-19. https://doi.org/10.1007/s10518-022-01347-6

Bathe, K. J., & Wilson, E. L. (1976). Numerical methods in finite element analysis. Prentice-Hall *Englewood Cliffs, NJ*, *2*.

Bertolesi, E., Milani, G., & Lourenço, P. B. (2016). "Implementation and validation of a total displacement non-linear homogenization approach for in-plane loaded masonry". *Computers & Structures*, 176, 13-33. https://doi.org/10.1016/j.compstruc.2016.08.001

Bianchini, N., Mendes, N., Lourenço, P.B., Calderini, C., Rossi, M. (2019). "Seismic assessment of masonry cross vaults through numerical nonlinear static and dynamic analysis". In: Papadrakakis M, Fragiadakis M (eds) COMPDYN 2019 7th ECCOMAS thematic conference on computational methods in structural dynamics and earthquake engineering, Crete, Greece, pp 600–612. https://doi.org/10.7712/120119.6942.18709

Bianchini, N., Mendes, N., Calderini, C. et al. (2022). "Seismic response of a small-scale masonry groin vault: experimental investigation by performing quasi-static and shake table tests". *Bulletin of Earthquake Engineering* 20, 1739–1765. https://doi.org/10.1007/s10518-021-01280-0

Bilko P, Małyszko L. (2020) "An Orthotropic Elastic-Plastic Constitutive Model for Masonry Walls". *Materials*. 13(18):4064. https://doi.org/10.3390/ma13184064

Blind Prediction Competition - Sera.ta - Seismic Response of Masonry Cross vaults: Shaking table tests and numerical validations. Blind prediction data, 2023. https://doi.org/10.5281/zenodo.7624666

Brincker, R., & Ventura, C. (2015). Introduction to operational modal analysis. John Wiley & Sons. https://doi.org/10.1002/9781118535141

Carfagnini, C., Baraccani, S., Silvestri, S., & Theodossopoulos, D. (2018). "The effects of in-plane shear displacements at the springings of Gothic cross vaults". *Construction and Building Materials*, *186*, 219-232. https://doi.org/10.1016/j.conbuildmat.2018.07.055

Cattari, S., Calderoni, B., Caliò, I. *et al.* (2022) "Nonlinear modeling of the seismic response of masonry structures: critical review and open issues towards engineering practice". *Bulletin of Earthquake Engineering* 20, 1939–1997. https://doi.org/10.1007/s10518-021-01263-1

CNR-DT 215/2018, Guide for the Design and Construction of Externally Bonded Fibre Reinforced Inorganic Matrix Systems for Strengthening Existing Structures.

Cundall, P. A., & Strack, O. D. (1979). "A discrete numerical model for granular assemblies". *geotechnique*, *29*(1), 47-65. https://doi.org/10.1680/geot.1979.29.1.47

D'Altri, A. M., Castellazzi, G., de Miranda, S., & Tralli, A. (2017). "Seismic-induced damage in historical masonry vaults: A case-study in the 2012 Emilia earthquake-stricken area". *Journal of Building Engineering*, *13*, 224-243. https://doi.org/10.1016/j.jobe.2017.08.005

Fagone, M., Rotunno, T., Bati, S.B. (2016). "The groin vaults of St. John Hospital in Jerusalem: an experimental analysis on a scale model". *International Journal of Architectural Heritage* 10(May):903–918. https://doi.org/10.1080/15583058.2016.1158331

Foti, D., Vacca, V., & Facchini, I. (2018). "DEM modeling and experimental analysis of the static behavior of a dry-joints masonry cross vaults". *Construction and Building Materials*, *170*, 111-120. https://doi.org/10.1016/j.conbuildmat.2018.02.202

Gaetani, A. (2020). *Seismic performance of masonry cross vaults: Learning from historical developments and experimental testing* (Vol. 91). Sapienza Università Editrice. ISBN 978-88-9377-144-3. https://doi.org/10.13133/9788893771443

Girardi, M., Padovani, C., & Pellegrini, D. (2019a). Modal analysis of masonry structures. *Mathematics and Mechanics of Solids*, 24(3), 616-636. https://doi.org/10.1177/1081286517751837

Girardi, M., Padovani, C., Pellegrini, D., & Robol, L. (2019b). Model updating procedure to enhance structural analysis in FE code NOSA-ITACA. *Journal of Performance of Constructed Facilities*, 33(4), 04019041. https://doi.org/10.1061/(ASCE)CF.1943-5509.0001303

Girardi, M., Padovani, C., Pellegrini, D., & Robol, L. (2021). A finite element model updating method based on global optimization. *Mechanical Systems and Signal Processing*, 152, 107372. https://doi.org/10.1016/j.ymssp.2020.107372

Gonen, S., Pulatsu, B., Lourenço, P. B., Lemos, J. V., Tuncay, K., & Erduran, E. (2023). Analysis and prediction of masonry wallette strength under combined compression-bending via stochastic computational modeling. *Engineering Structures*, 278, 115492. https://doi.org/10.1016/j.engstruct.2022.115492

Lengyel, G., & Németh, R. K. (2018). "The mechanical behavior of ribs in masonry groin vaults subjected to seismic load". *International Journal of Architectural Heritage*. https://doi.org/10.1080/15583058.2018.1491652

Lourenço, P. B., & Gaetani, A. (2022). *Finite Element Analysis for Building Assessment: Advanced Use and Practical Recommendations*. Taylor & Francis. eBook ISBN 9780429341564 https://doi.org/10.1201/9780429341564

Lucchesi, M., Padovani, C., Pasquinelli, G., & Zani, N. (1999). "The maximum modulus eccentricities surface for masonry vaults and limit analysis". *Mathematics and Mechanics of Solids*, 4(1), 71-87. https://doi.org/10.1177/108128659900400105

Lucchesi, M., Padovani, C., Pasquinelli, G., & Zani, N. (2008). *Masonry constructions: mechanical models and numerical applications*. Springer Science & Business Media. https://doi.org/10.1007/978-3-540-79111-9

Malomo, D., & DeJong, M. J. (2022). "A Macro-Distinct Element Model (M-DEM) for simulating in-plane/out-of-plane interaction and combined failure mechanisms of unreinforced masonry structures". *Earthquake Engineering & Structural Dynamics*, 51(4), 793-811. https://doi.org/10.1002/eqe.3591

Masi, F., Stefanou, I., Maffi-Berthier, V., & Vannucci, P. (2020). "A Discrete Element Method based-approach for arched masonry structures under blast loads". *Engineering Structures*, *216*, 110721. https://doi.org/10.1016/j.engstruct.2020.110721

Mendes N., Lourenço P.B. (2014). Sensitivity analysis of the seismic performance of existing masonry buildings. *Engineering Structures*, 80:137–146. https://doi.org/10.1016/j.engstruct.2014.09.005

Milani, G., Valente, M., Fagone, M., Rotunno, T., & Alessandri, C. (2019). "Advanced non-linear numerical modeling of masonry groin vaults of major historical importance:

St John Hospital case study in Jerusalem". *Engineering Structures*, *194*, 458-476. https://doi.org/10.1016/j.engstruct.2019.05.021

NTC2018 - Ministero delle Infrastrutture e dei Trasporti "Aggiornamento delle Norme tecniche per le costruzioni". Decreto 17 gennaio 2018.

Nodargi, N. A., & Bisegna, P. (2019). "A mixed finite element for the nonlinear analysis of in-plane loaded masonry walls". *International Journal for Numerical Methods in Engineering*, *120*(11), 1227-1248. https://doi.org/10.1002/nme.6179

Parisse F., Cattari S., Marques R., Lourenço P.B., Magenes G., Beyer K., Bruno Calderoni M., Karakaya D.M., Manzini C.F. (2021). Benchmarking the seismic assessment of unreinforced masonry buildings from a blind prediction test. *Structures* 31:982–1005. https://doi.org/10.1016/j.istruc.2021.01.096

Pellegrini, D., Girardi, M., Lourenço, P. B., Masciotta, M. G., Mendes, N., Padovani, C., & Ramos, L. F. (2018). Modal analysis of historical masonry structures: Linear perturbation and software benchmarking. *Construction and Building Materials*, 189, 1232-1250. https://doi.org/10.1016/j.conbuildmat.2018.09.034

Petracca, M., Pelà, L., Rossi, R., Oller, S., Camata, G., & Spacone, E. (2017). "Multiscale computational first order homogenization of thick shells for the analysis of out-of-plane loaded masonry walls". *Computer Methods in Applied Mechanics and Engineering*, *315*, 273-301. https://doi.org/10.1016/j.cma.2016.10.046

Post-diction Competition - Sera.ta - Seismic Response of Masonry Cross vaults: Shaking table tests and numerical validations. Post diction data, 2023. https://doi.org/10.5281/zenodo.7624791

Pulatsu, B., Gencer, F., & Erdogmus, E. (2020). "Study of the effect of construction techniques on the seismic capacity of ancient dry-joint masonry towers through DEM". *European Journal of Environmental and Civil Engineering*, 1-18. https://doi.org/10.1080/19648189.2020.1824823

Regan, O. M., Bourgeois, E., Colas, A. S., Chatellier, P., Desbordes, A., & Douroux, J. F. (2017). "Application of a coupled homogenization-damage model to masonry tunnel vaults". *Computers and Geotechnics*, *83*, 132-141. https://doi.org/10.1016/j.compgeo.2016.10.024

Sarhosis, V., Lemos, J. V., & Bagi, K. (2019). "Discrete element modeling". *Numerical modeling of masonry and historical structures*, 469-501. https://doi.org/10.1016/B978-0-08-102439-3.00013-0

Silvestri, S., Baraccani, S., Foti, D., Ivorra, S., et al. (2021). "Shaking table testing of groin vaults made by 3D printers". *Soil Dynamics and Earthquake Engineering*, Volume 150, 106880, ISSN 0267-7261. https://doi.org/10.1016/j.soildyn.2021.106880

Stefanou, I., Sab, K., & Heck, J. V. (2015). "Three dimensional homogenization of masonry structures with building blocks of finite strength: A closed form strength

domain". *International Journal of Solids and Structures*, *54*, 258-270. https://doi.org/10.1016/j.ijsolstr.2014.10.007

Vadalà, F., Cusmano, V., Funari, M. F., Caliò, I., & Lourenço, P. B. (2022). "On the use of a mesoscale masonry pattern representation in discrete macro-element approach". *Journal of Building Engineering*, *50*, 104182. https://doi.org/10.1016/j.jobe.2022.104182

Van Mele, T., Mcinerney, J., Dejong, M. And Block, P. (2012). "Physical and computational discrete modelling of masonry vault collapse". In Jasieńko, J. (ed.) *Structural Analysis of Historical Constructions*, Vols 1-3. Wrocław, pp. 2552–2560